Chemical Physics 366 (2009) 2–8

Contents lists available at ScienceDirect

Chemical Physics

journal homepage: www.elsevier.com/locate/chemphys

4D attosecond imaging with free electrons: Diffraction methods and potential applications

Peter Baum [a,*], Ahmed H. Zewail [b,*]

[a] Max-Planck-Institute of Quantum Optics, and Ludwig-Maximilians-Universität München, Am Coulombwall 1, 85748 Garching, Germany
[b] Physical Biology Center for Ultrafast Science and Technology, Arthur Amos Noyes Laboratory of Chemical Physics, California Institute of Technology, Pasadena, CA 91125, USA

ARTICLE INFO

Article history:
Received 30 May 2009
Accepted 28 July 2009
Available online 8 August 2009

Keywords:
Attosecond imaging
Electron dynamics

ABSTRACT

We consider here the extension of four-dimensional (4D) electron imaging methodology to the attosecond time domain. Specifically, we discuss the generation of attosecond electron pulses and the *in situ* probing with electron diffraction. The free electron pulses have a de Broglie wavelength on the order of picometers and a high degree of monochromaticity ($\Delta E/E_0 \approx 10^{-4}$); attosecond optical pulses have typically a wavelength of 20 nm and $\Delta E/E_0 \approx 0.5$, where E_0 is the central energy and ΔE is the energy bandwidth. Diffraction, and tilting of the electron pulses/specimen, permit the direct investigation of electron density changes in molecules and condensed matter. We predict the relevant changes in diffraction caused by electron density motion and give two examples as prototype applications, one that involves matter-field interaction, and the other is that of change in bonding order. This 4D imaging on the attosecond time scale is a pump–probe approach in free space and with free electrons.

1. Introduction

The relevant length and time scales of electron–nuclear motions are determined by the forces and masses within the structures of interest. For atomic movements, quantum principles dictate the time and distance scales of femtoseconds and angstroms. Slower and larger-scale dynamics, which are governed by such motions, are equally important for a variety of processes. A full picture of the change requires observation throughout the hierarchy of scales [1].

Electron dynamics occur in the attosecond–femtosecond domain [2–6] and are different in their manifestations from those involving nuclear motions, the bond making and bond breaking events of femtochemistry [7]. For example, electron displacement out of the equilibrium position in materials is the microscopic origin of light emission, refractive index, current, plasmon and polariton activity, and of nonlinear optical effects. Moreover, electron density distributions, if possible to follow, can mirror changes in bonding/anti-bonding description of the orbitals involved. The imaging of such changes, therefore, requires both the time and space resolution.

Optical attosecond pulses have already been advanced to measure femtosecond Auger decays [8], femtosecond dynamics of diatomics [9–12], and the attosecond delay due to the speed difference of free electrons in solids [13]; for comprehensive review see [2]. One approach that aims at the probing of electron density of orbitals is that of Corkum and coworkers [6,14]. In these, so far, static experiments, ionization is first made by a strong laser field, and because the electrons resulting from ionization are re-accelerated back to the ions, the emitted radiation indirectly reflects the remaining electron density distribution. This was reported for a diatomic [14] with the interpretation aided by knowledge of the initial electronic structure, which depends on the system complexity [15,16]. Several theoretical studies have indicated the time scales involved for electron dynamics in more complex systems [17–19]. It should be noted that the sensitivity of spectroscopic studies with attosecond optical pulses [20] is determined by a significant change of the transition probability or by a shift of the transition energy by many eV. Thus, changes of charge distributions that have small energy shifts become unobservable.

In this contribution, we focus on a different methodology for attosecond science, namely the extension of ultrafast 4D diffraction and microscopy [21] to the attosecond regime. The key concept here is the use of attosecond electron diffraction to observe attosecond electron motion. We show that in order to achieve such visualization methodology the pulses have to be freely generated, compressed, and tilted. The approach can be implemented to extend previous studies from Caltech, for example those of phase transformations [22,23], chemical reactions [21], nano-mechanical processes [24,25], and surface dynamics [26,27], and possibly to other studies (in other laboratories) of melting processes [28,29], coherent phonons [30], gold particles [31], and molecular alignment [32].

* Corresponding authors.
E-mail addresses: peter.baum@lmu.de (P. Baum), zewail@caltech.edu (A.H. Zewail).

0301-0104/$ - see front matter © 2009 Elsevier B.V. All rights reserved.
doi:10.1016/j.chemphys.2009.07.013

Earlier, we discussed schemes for obtaining attosecond resolution with electron diffraction [33] with focus on the generation of pulses. Here we present, besides the generation, the *in situ* probing through diffraction with free electrons, and give two possible prototypical applications. Three key points must be addressed: first, attosecond diffraction requires near mono-energetic attosecond electron pulses for keV-range of energies in free space, and thus space charge effects need to be considered. Second, spatio-temporal synchronization of the electron pulses to the pump pulses must be made along the entire sample area and with attosecond precision. Third, diffraction orders must be shown to be sensitive to the effect of electron displacement and conclusive of the four-dimensional dynamics. In the following sections, we shall discuss the methodology and then highlight possible applications and pump–probe schemes.

2. Attosecond resolution in electron diffraction

A central requisite for reaching attosecond resolution with electron diffraction is the generation of attosecond electron pulses in 'free space', so that diffraction from freely chosen samples of interest can take place independent of the mechanisms of pulse generation. Electrons with energies of 30–300 keV are ideal for imaging and diffraction, because of their high scattering cross sections, convenient diffraction angles, and the appropriate de Broglie wavelength (0.02–0.07 Å) to resolve atomic-scale changes. Moreover, they have a high degree of monochromaticity. For example, electrons accelerated to $E_0 = 30$–300 keV with pulse duration of 20 attoseconds (bandwidth of $\Delta E \approx 30$ eV) have $\Delta E/E_0 \approx 10^{-3}$–$10^{-4}$, making diffraction and imaging possible without a spread in angle and resolution. Optical attosecond pulses have typically $\Delta E/E_0 \approx 0.5$ [34,35] and because of this reach of ΔE to E_0, their duration is Fourier-limited to ~100 attoseconds [34,35]. Free electron pulses of keV central energy can, in principle, have much shorter duration, down to sub-attoseconds, while still consisting of many wave cycles [33].

2.1. Single electron packets and dispersion

Pulses with a large number of electrons suffer from the effect of space charge, which determines both the spatial and the temporal resolutions. This can be avoided by using packets of single, or only a few, electrons in a high repetition rate, as demonstrated in 4D microscopy imaging [36]. Fig. 1 depicts the relation of single electron packets to the effective envelope due to statistics. A second obstacle is the high dispersion for electrons of non-relativistic energy. The small but unavoidable bandwidth of an attosecond electron pulse causes the pulse to disperse during propagation in free space, even when no space charge forces are present. For example, a 20-attosecond pulse with $\Delta E/E_0 \approx 10^{-3}$ would stretch to picoseconds after just a few centimeters of propagation.

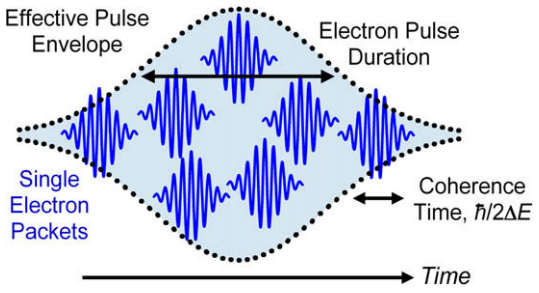

Fig. 1. Single-electron packets and electron pulses. Shown are the effective macroscopic pulse parameters and the coherence time involved. Each single electron (blue) is a coherent packet consisting of many cycles of the de Broglie wave and has different timing due to the statistics of generation. On average, multiple single electron packets form an effective electron pulse (dotted envelope).

Our approach for the suppression of dispersion and the generation of free attosecond electron pulses is based on the initial preparation of negatively-chirped electron packets [33]. In this approach, femtosecond electron pulses are generated by photoemission and accelerated to keV energies in a static electric field. Preceding the experimental interaction region, optical fields are used to generate electron packets with a velocity distribution, such that the higher-energy parts are located behind the lower-energy ones. With a proper adjustment of this chirp, the pulse then self-compresses to extremely short durations while propagating towards the point of diffraction. To achieve attosecond pulses, the chirp must be imprinted to the electron pulse on a nanometer length scale. Optical waves provide such fields. However, non-relativistic electrons move significantly slower than the speed of light (e.g. ~0.3 c for 30 keV). The direct interaction with an optical field will, therefore, cancel out over time and can not be used to accelerate and decelerate electrons for compression. In order to overcome this limitation, we make use of the ponderomotive force, which is proportional to the gradient of the optical intensity to accelerate electrons out of regions with high intensity. By optical wave synthesis, intensity profiles can be made that propagate with less than the speed of light and, therefore, allow for co-propagation with the electrons.

Fig. 2 depicts a schematic of the concept. A synthesized optical field of two counter-propagating waves of different wavelengths results in an effective intensity grating, similar to a standing wave, which moves with a speed slower than the speed of light. Electrons can, therefore, co-propagate with a matched speed and are accelerated or decelerated by the ponderomotive force according to their position within the wave. After the optical fields have completely faded away, this velocity distribution results in self-compression; the attosecond pulses are formed in free space and away from the spatial region of the laser fields. Depending on the optical pulse intensity, the electron pulse duration can be made as short as 15 attoseconds [33], and, in principle, shorter durations are achievable. If the longitudinal spatial width of the initial electron pulse is longer than the wavelength of the intensity grating, multiple attosecond pulses emerge that are located with well-defined spacing at

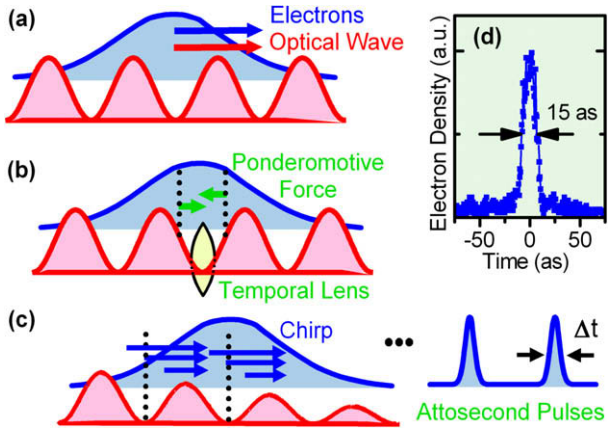

Fig. 2. Temporal optical gratings for the generation of free attosecond electron pulses for use in diffraction [33]. (a) A femtosecond electron packet (blue) is made to co-propagate with a moving optical intensity grating (red). (b) The ponderomotive force pushes electron towards the minima and thus creates a temporal lens [37]. (c) The induced electron chirp leads to compression to attosecond duration at later time. (d) The electron pulse duration from 10^5 trajectories reaches into the domain of few attoseconds.

the optical minima. This concept of compression, which was tested by simulation [33], can be rigorously described analytically as a 'temporal lens effect' [37]. The temporal version of the Kapitza–Dirac effect [38–40] has an interesting analogy.

Some of the simulations in our initial work were based on an effective ponderomotive force in a collinear geometry. In order to extend the approach to more complex arrangements, here we generalize the approach and consider the full spatiotemporal (electric and magnetic) fields of two colliding laser waves with an arbitrary angle and polarization. The transversal and longitudinal fields of a Gaussian focus were applied [41]. We simulated electron trajectories by applying the Lorentz force with a fourth-order Runge–Kutta algorithm using steps of 100 attoseconds. The spatial dimensions were treated exactly, in order to correctly capture the compression of electron packets into extremely small volumes. Space charge effects were taken into account by calculating the Coulomb interactions between all single electrons for each time step (N-body simulations).

As a first check, our earlier findings for exactly counter-propagating laser beams were reproduced, and the same electron compression dynamics and final attosecond pulse durations were obtained; the optical polarization has no effect as long as the counter-propagating waves can interfere. We then considered the more general case. Fig. 3 depicts the compression of radially extended electron packets in the combined field of two counter-propagating laser pulses with durations of 300 fs at wavelengths of 1040 nm and 520 nm, with ~5 μJ each. The plotted pulse shape is a statistical average over 10^5 packets of single electrons (see Fig. 1). The beam diameter of the initial electron packet was 10 μm and the beam diameters of the laser pulses were 60 μm; the resulting compression dynamics is depicted before, just at, and some time after the time of best compression to a duration of 15 attoseconds (see Fig. 3b). These results show that an optical wave with a beam diameter of only several times larger than that of the electron packet is sufficient to result in almost homogeneous compression across the entire electron beam. The characteristic longitudinal spread after the point of best compression, as depicted in Fig. 3c, is result of the histogram of accelerations along the sinusoidal laser wave. Most electrons are accelerated or decelerated, and only a small fraction is not affected. The energy spectrum of the compressed electron pulse, accordingly, has a shape similar to the letter 'M'.

2.2. Space charge effects

Coulomb forces prevent concentration of a large number of electrons in a limited volume, and a compromise between electron flux and laser repetition rate must be found to achieve sufficiently intense diffraction. The laser pulses for compression have energies on the order of 5 μJ and can, therefore, be generated at MHz repetition rates with the resulting flux of 10^6 single electrons/s, which is sufficient for conclusive diffraction. Nevertheless, having more than one electron per attosecond pulse is beneficial for improving the total flux.

In order to investigate the influence of space charge on the performance in our attosecond compression scheme, we considered electron packets of increasing electron density and evaluated the resulting pulse durations and effective electron density per attosecond pulse. Two findings are relevant with the results shown in Fig. 4. First, the duration of individual attosecond electron pulses increases relatively insignificantly with the number of electrons contained within. Even for 40 electrons in a single pulse, the duration increases only from 15 to 25 attoseconds (see Fig. 4a). The reasons for this are the highly oblate shape of the electron pulses, and the approximate linearity of space charge forces in the longitudinal direction, which are compensated for by somewhat longer interaction in the ponderomotive forces of the optical waves.

Secondly, for a train of pulses, there is an effect on synchronization. When the initial femtosecond electron packet covers several optical cycles of the compression wave (see Fig. 1), a train of attosecond pulses results. Perfect synchronization to the optical wave is provided, because all attosecond pulses are located at the same optical phase of the fundamental laser wave [33]. This phase matching relation, which permits attosecond resolution despite the presence of multiple pulses, is altered under space charge conditions. The attosecond pulses repel each other and a temporal spreading of the comb-like train results. For a train of 10 attosecond pulses, Fig. 4b displays the difference in timing for an adjacent attosecond pulse in relation to the central one, which is always locked to the optical phase because the space charge forces cancel out. The total timing mismatch is the product of the plotted value with the number of attosecond pulses in the entire electron packet (10 for this example). In order to keep the total mismatch to the optical wave below 20 attoseconds, 10 electrons per attosecond electron pulse represent an optimum value. The total pulse train then consists of 200 electrons for that group of pulses; of course the total flux of electrons is determined by the repetition rate. Note that mismatch to the compression wave is absent with isolated attosecond electron pulses, which are generated when the initial uncompressed electron packet is shorter than a few femtoseconds, and/or with optical fields of longer wavelength.

Numerous imaging experiments have been successful with single electron packets [21,42]. In state-of-the-art electron crystallography experiments, typically 500 electrons per pulse were used at a repetition rate of kHz [22] to produce the needed diffraction. This is equivalent to having five electrons per attosecond pulse at 100 kHz, which is a convenient repetition rate for optical wave synthesis, and provides enough time for letting the material under investigation cool back to the initial state. Laser systems with MHz repetition rates will provide even higher fluxes.

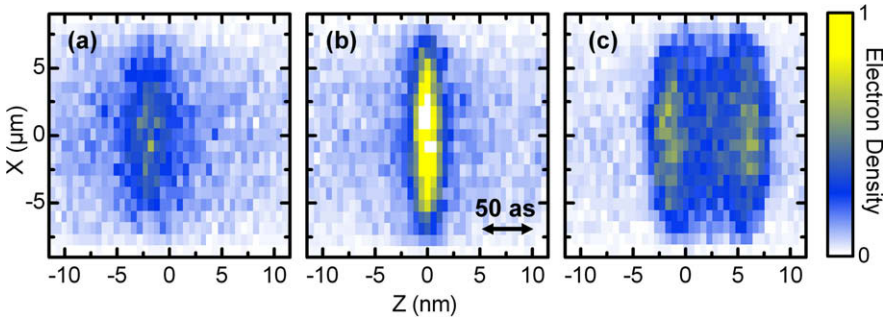

Fig. 3. Spatiotemporal compression dynamics of attosecond electron pulses averaged over 10^5 single trajectories. *Z* is the propagation direction and *X* is perpendicular. The pulse is shown just before, at, and after the time of best compression; the center along *Z* is shifted for clarity.

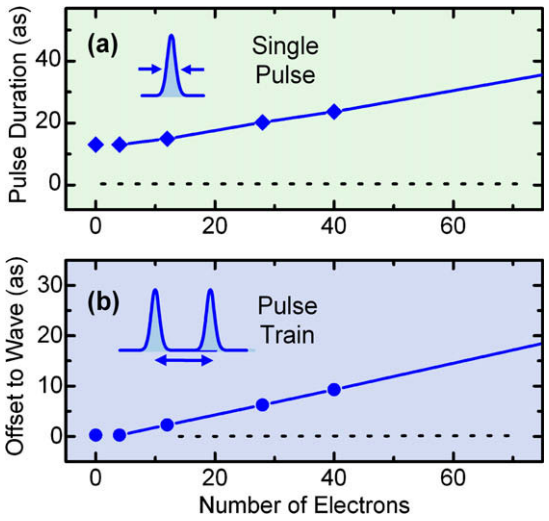

Fig. 4. Space charge effects on pulse width and synchronization. (a) The attosecond pulse duration increases with the number of electrons within the attosecond pulses. (b) For the case of multiple pulses, space charge repulsion affects the synchronization to the minima of the optical wave. Adjacent pulses accumulate a temporal offset to each other (see text).

2.3. Space–time phase matching with tilted attosecond pulses

Applications of attosecond electron pulses for diffraction and microscopy require synchronization of events in the pump–probe arrangement with an accuracy that is equal or better than the individual pulse durations. In contrast to recompression concepts that are based on time-dependent microwave fields [43–45], the application of laser waves for attosecond electron pulse generation provides exact temporal synchronization when the pump pulses are derived by phase-locking from the same laser system. Many common optical techniques, such as nonlinear frequency conversion, continuum generation in solids [46,47], or high-harmonic generation [34,35], all provide a phase lock in the sense that the outcome has the same relative phase and timing in relation to the incoming optical wave for each single pulse of the laser.

A second requirement for reaching into the temporal resolution of attoseconds is the realization of spatial delay matching along extended areas of the diffraction [48]. The use of large samples, for example with up to millimeters in size in some experiments, provides enhanced diffraction efficiency and offers the possibility to use electron beams with large diameter, in order to maximize the coherence and flux. In this case, the time resolution is limited by differences in the arrival times of pump and probe pulses at different points within the involved beam diameters (group velocity mismatch).

Electron pulses at keV energies travel with significantly less than the speed of light (e.g. $v_{el} = 0.3\ c$ for 30 keV electrons) and are, therefore, 'overtaken' by the laser wave. However, in a collinear geometry, the multiple attosecond electrons pulses within a pulse train arrive at a given sample location with temporal coincidence to the phase of the original laser wave, because the electron pulses are generated with a spacing that is more narrow than the laser wavelength. The velocity matching condition for compression leads to distances between the individual electron pulses that just compensate for the slower speed [33]. If the compression wave is properly synthesized, the simulations show that all electron pulses in a pulse train hit the target with the same frequency as the laser carrier wave and have therefore a fixed phase relation. Also, fluctuations of the optical carrier-envelope phase cancel out.

A collinear arrangement is not beneficial for many applications. We here offer two novel schemes for matching the group velocity of electrons with the phase velocity of optical pulses, which are suitable for applications in non-collinear, ultrafast electron microscopy and diffraction. Fig. 5a presents a concept for the transmission geometry in which two angles are introduced, one between the laser beam and the electron beam (β), and another one (α) for the tilt angle of the sample (black) to the phase fronts of the laser wave. Total synchrony is achieved if the relative delay between the optical wave and the attosecond electron pulses is made identical for all points along the entire sample surface. Each small volume of the sample is then subject to an individual pump–probe-type experiment with the same time delay. The sample thickness in electron diffraction and microscopy is below μm and does not significantly affect the phase matching.

The above condition is found when we match the coincidence along the width of the specimen. The effective surface velocity $v_{surface}$ of the laser and of the electron pulses must be identical. From Fig. 5a, this requirement is expressed by the following equation:

$$\frac{\sin(\alpha)}{\sin(\alpha-\beta)} = \frac{c}{v_{el}}. \tag{1}$$

It follows that an angle of $\beta = 10°$, for example, results in an optimum angle for the sample tilt of $\alpha = 14.8°$, which are both easily achievable angles in a real experiment. The effective tilt of the sample with respect to the electron direction is then $\alpha - \beta = 4.8°$. Naturally, if this value is not coincident with a zone axis direction, a complete rocking curve should be obtained in order to optimize α and β with tilt requirements.

Another option for synchronization along extended surfaces is the use of tilted electron pulses, for that the electron density makes an angle with respect to the propagation direction. Tilted optical pulses were used for reaching femtosecond resolution in reflection geometry [48], but here tilted electron pulses are introduced for effective spatiotemporal synchronization to the phase velocity of the excitation pulses along the entire sample surface. Fig. 5b depicts the concept. If an angle γ is chosen between the laser (red) and the attosecond electron pulses (blue), the electron pulses need to be tilted likewise. The sample is located parallel to the optical phase fronts and its entire surface is illuminated by the attosecond electron pulse at once and at the same time of incidence relative to the optical pulse wave. Because the incidence is delay-free for all points along the surface, velocity matching is provided for the whole probed area.

The generation of tilted attosecond electron pulses is outlined in Fig. 6a. As described above, a femtosecond electron packet (blue) is

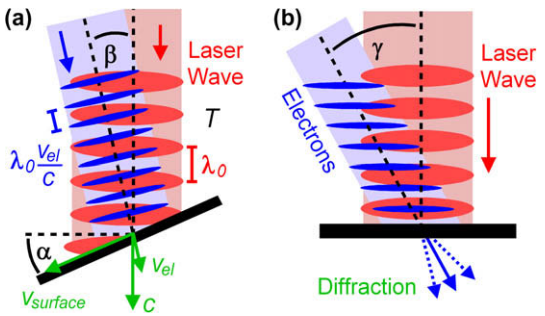

Fig. 5. Schemes for phase matching of laser phase fronts (red) and electron pulses (blue) at extended specimen areas (black). (a) An arrangement for synchronization by adjusting the appropriate angles between laser and electron beams in combination with sample tilt (see text). (b) Alternatively, tilted attosecond electron pulses allow the instantaneous probing of the entire surface.

first generated by conventional photoelectron generation and accelerated in a static electric field. By intersecting the counter-propagating intensity grating at an angle, tilted electron pulses result with attosecond duration. The ponderomotive force accelerates the electrons towards the planes of destructive interference in the intensity wave and they form attosecond pulses that are compressed along the optical beam axis; but the pulses propagate in the original direction. Only a slight adjustment of the electrons' central energy is required to achieve phase matching to the moving optical grating [33].

Based on this concept, we simulated the tilting effect by using 31-keV electron pulses with an initial duration of ~15 femtoseconds and a spatial beam diameter of ~10 μm (Fig. 6b, left). The optical intensity wave is synthesized by two counter-propagating laser pulses of 100-fs duration and wavelengths of 1040 and 520 nm. The angle between the electron beam and the laser wave is 5°. The results of compression are shown in Fig. 6b: As expected, attosecond electron pulses are formed at the minima of the optical intensity wave and, therefore, are tilted by 5° with respect to the electron propagation direction. For other incidence angles of the laser, the electron pulses are tilted accordingly. Perpendicular to the attosecond pulses (see Fig. 6), the measured duration is ~20 attoseconds, given as the full width at half maximum.

3. Attosecond 4D imaging: applications

Having outlined the methodology for generation and synchronization of attosecond electron pulses, we now consider the diffraction and manifestation of electron dynamics in the patterns. By way of two different examples, we outline the conditions for observing electronic motions in molecules and materials with attosecond electron packets.

3.1. Scattering factors

In this section, we consider first the physics of electron scattering and the change in scattering factors which characterize individual atoms and the electron density involved. Diffraction from molecular crystals or other crystalline structures provides two distinct advantages over that obtained for gas phase ensembles. First, the sample density is many orders of magnitudes higher (10^{20} molecules/cm^3 as compared to 10^{10}–10^{16}/cm^3 in gas jets); diffraction is, therefore, more intense. Second, the crystalline order results in Bragg scatterings that are concentrated into well-defined 'spots' for ordered crystals; the patterns become rods for surfaces and narrow rings for amorphous substances. The diffraction results in intensities which are proportional to the square of the diffraction amplitude. As discussed below, coherence in diffraction is critical for observing the changes of interest.

The diffraction from molecular crystals, or other crystalline materials, is defined by the summation over the contributions of all scatterers in a unit cell. The intensity I of a Bragg spot with the Miller indices (hkl) is determined by the positions (xyz) of the scatterers j in the unit cell:

$$I(hkl) \propto \left| \sum_j f_j \exp\left[-2\pi i\ (hkl)\cdot(xyz)_j\right] \right|^2, \tag{2}$$

where f_j are the atomic scattering factors. Electron diffraction is the result of Coulomb interaction between the incoming electrons and the potential formed by nuclei and electrons. The factors f_j account for the effective scattering amplitude of atoms and are derived from quantum calculations that take into account the specific electron density distribution around the nuclei, including core electrons. The scattering we are considering here is the elastic one.

In order to estimate the influence of electron dynamics on contributions to time-resolved diffraction patterns, we consider typical densities of electrons in chemical bonds, and the possible change. Static electron density maps show that typical covalent bonds consist of about one electron/Å^3 and that this density is delocalized over volumes with diameters in the order of 1 Å [49]. For estimating an effective scattering factor of such electron density, we consider a Gaussian sphere with a diameter of 1 Å, consisting of one electron. The electric potential is derived by Gauss' law and results in a radial dependence that is represented in Fig. 7a, dotted line. The total scattering amplitude of free charges diverges at small angles, because of the long-range behavior of the potential [50]. Since in real crystals the potential is localized in unit cells, we use a Gaussian distribution of the same magnitude in order to restrict the range to about ±1.5 Å.

For potential of spherical symmetry, an effective scattering factor can be calculated from the radial potential $\Phi(r)$ according to

$$f_{el}(s) = \frac{8\pi^2 m_e e}{h^2} \int_0^\infty r^2 \Phi(r) \frac{\sin(4\pi s r)}{4\pi s r} dr, \tag{3}$$

where $s = \sin(\vartheta/2)/\lambda_{el}$ is the scattering parameter for a diffraction angle ϑ and λ_{el} is the de Broglie wavelength of the incident electrons

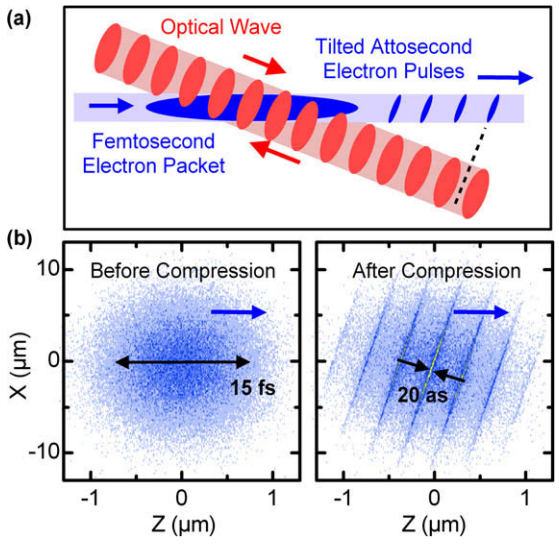

Fig. 6. Generation of tilted electron pulses. (a) The introduction of an angle between the intensity grating (red) and the electron beam (blue) leads to formation of electron pulses with a tilt. (b) Simulation results for an initial packet of 15-femtosecond duration (left) and an intersection angle of 5°. The tilted attosecond pulses have duration of ~20 attoseconds when measured perpendicular to the tilt (note the different scale of Z and X).

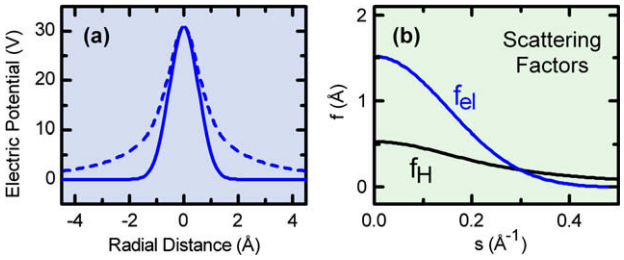

Fig. 7. Scattering factor of electron density distributions. (a) Potential of a Gaussian electron density (dotted) and approximate one (solid) made in order to reduce the unphysical long-range interaction (see text). (b) Effective scattering factors for a Gaussian electron density (blue). The scattering of hydrogen is given for comparison (black).

[50]. The result for our delocalized electron density is shown in Fig. 7b; for comparison we plot also the tabulated scattering factor of neutral hydrogen [50]. Both have comparable magnitude, which is expected because of their similar sizes.

3.2. Molecular excitations

Here, we consider the iodine molecule as a model case and invoke the transition from a bonding to an anti-bonding orbital. The crystal structure of iodine consists of nearly perpendicular iodine pairs with a bond length of ~2.7 Å [51]. Two electrons contribute to the intramolecular σ bond; the intermolecular bond is weaker [52].

Fig. 8a depicts the system under study. The effect of anti-bonding excitation is made by comparing the Bragg intensities for the iodine structure, including the binding electrons, to a hypothetical iodine crystal consisting only of isolated atoms (see Fig. 8a). In Table 1a, we give the results of the calculations following Eq. (2) with the values of f tabulated for iodine atoms [50] and from Eq. (3) for the electronic distribution changes. Despite the large difference in f of the iodine nuclei and the electron (about 50:1), the changes of Bragg spot intensity are significant, being on an order of 10–30%.

This large change is for two reasons. First, the bonding electrons are located in-between iodine atoms and contribute, therefore, strongly to the enhancement or suppression of all Bragg spots that project from the inter-atomic distances of the molecular units. Second, the large effect is result of the intrinsic 'heterodyne detection' scheme of diffraction; the total intensity of a Bragg spot scales with the square of the coherent sum of individual contributions (see Eq. (2)). Although the total contribution to the intensity of a Bragg spot from bonding electrons is lower by a factor of several hundreds than the intensity contributions from the iodine atoms, the modulation is on the order of several percents as a result of the coherence of diffraction on a nanometer scale [53]. Symmetry in the crystal is evident in the absence of change in certain Bragg orders. From measurements of the dynamics of multiple spots, it follows that electron density movies could be made. This is best achieved in an electron microscope in diffraction geometry; however conventional diffraction is also suitable to simultaneously monitor many Bragg spots [22] and is advantageous for the study of ordered bulk materials. The example given is not far from an experimental observation made on an ultrafast metal-to-insulator transition for which a σ^*-type excitation was induced with a femtosecond pulse [22].

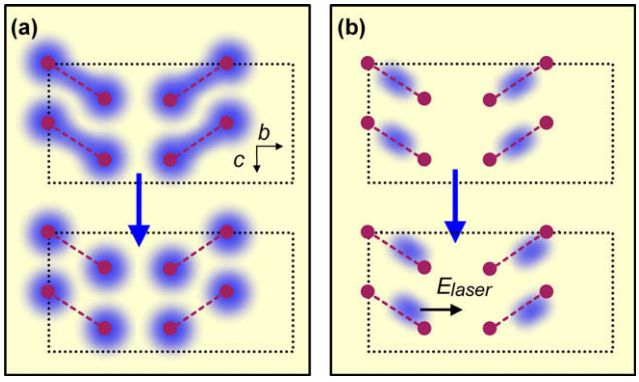

Fig. 8. Schematic for the two considered applications of 4D imaging with attosecond electron diffraction. (a) Transition of bonding order. (b) Displacement and oscillation of electron density in non-resonant laser fields. For explanation see text.

Table 1
Effects of electron motion on selected molecular Bragg spots.

Miller indices (*hkl*)	(a) $\Delta I_{\text{Transition}}$	(b) $\Delta I_{\text{Movement}}$ (0.08 Å)
100, 010, 001	(forbidden)	(forbidden)
200, 400, 600	0	0
002	+35%	0
020 (weak)	−50%	−17%
400	0	0
040	+18%	+13%
004	0	0
111	−15%	−2%
331	+20%	+15%

(a) Magnitude of Bragg spot intensity change ΔI of crystalline iodine as a result of bonding to anti-bonding transition. (b) Magnitude of Bragg spot intensity change as a result of field interaction with charge density, also in iodine.

3.3. Physical electron oscillations and resonances

As a second model case we consider the reaction of bonded electron density to external electric fields, such as the ones from laser fields (see Fig. 8b). Depending on the restoring force and the resonance, an electron density will oscillate with the driving field in phase or with a phase delay. This charge oscillation re-radiates and is responsible for the refractive index of a dielectric material. In order to estimate the magnitude of charge displacement, we take into account the polarizability, α, and the electric field strength, E_{laser}. In the limit of only one moving charge, the displacement D is approximately given by

$$D \approx \frac{\alpha}{e} E_{laser}. \tag{4}$$

The polarizability of molecular iodine along the bond is $\alpha \approx 130\ \varepsilon_0 \text{Å}^3$ (~70 a.u.) in the static limit and a similar magnitude is expected for the crystal for optical frequencies away from the strong absorption bands [54]; the anisotropy of polarizability indicates the role of the bonding electrons. With femtosecond laser pulses, a field of $E_{laser} = 10^9$ V/m is possible for intensities below the damage threshold; for example, 10^9 V/m correspond to ~10 mJ/cm^2 for a 30-fs pulse. With these parameters, one expects a charge displacement of $D \approx 0.08$ Å, or about 3% of the bond length.

Fig. 8b is a schematic for the change in charge distribution by an electric field. We assume an active role of only the bond electrons, and take the polarization of the laser field to be along the b axis of solid iodine. This axis is chosen because it has the least symmetry; a is perpendicular to the bonds. Table 1b gives the intensity changes of selected Bragg spots; the change is in the range of ±15% for some of the indices. The total energy delivered to the molecular system by the laser field is only on the order of 0.01 eV. Nevertheless the changes of charge displacements on sub-angstrom scales are evident. This marks a central advantage of electron diffraction over spectroscopic approaches, which require large energy changes in order to have projections on dynamics. In contrast, diffraction allows for the direct visualization of a variety of ultrafast electron dynamics with combined spatial and temporal resolutions, and independent of the resolution of internal energy levels.

4. Outlook

The above results suggest that 4D imaging methods with diffraction have the potential of revealing electron dynamics on the attosecond time scale. Given the proposed pump–probe experiments with free attosecond electrons, the issue of the pump characteristics must be considered. In femtoscience, especially femtochemistry and femtobiology, the pump-pulse energy width

is a small fraction of the dissociation energy of molecules and the dynamics is that of a nuclear motion in a given force field (electronic state). For the attosecond regime, because of the uncertainty in energy (>10 eV), such conditions are not met.

Here, we suggest three different avenues of pump–probe studies with diffraction. The first is to use ultraviolet or soft X-ray pump pulses that coherently cover multiple electronic states to form an electronic wave packet, the analogue of a nuclear packet. Charge density of some superposition will rapidly oscillate in a frozen nuclear framework. Because diffraction is insensitive to the resolution of states, it can follow the dynamics of possible electron–electron interactions and transient repulsion effects. The second approach would be to excite a well-defined state with a few-femtosecond pulse duration and then map the electronic distribution changes on this time scale while the nuclear motion is proceeding. The third prospect, as outlined above, is the study of 'off-resonance' effects due to electron displacements and oscillations, which are responsible for physical properties such as the refractive index and nonlinear optical effects. In all such scenarios, diffraction with free electron packets allows for four-dimensional imaging of charge density, independent of the mechanism of pulse generation.

Acknowledgements

This work was supported by the Rudolf-Kaiser-Stiftung, the Munich-Centre for Advanced Photonics, and by the National Science Foundation, the Air Force Office of Scientific Research, and the Gordon and Betty Moore Center for Physical Biology at Caltech. We thank C. Homann for his help with parallel computing.

References

[1] M. Chergui, A.H. Zewail, Chem. Phys. Chem. 10 (2009) 28.
[2] F. Krausz, M. Ivanov, Rev. Mod. Phys. 81 (2009) 163.
[3] P.B. Corkum, F. Krausz, Nat. Phys. 3 (2007) 381.
[4] M.F. Kling, M.J.J. Vrakking, Annu. Rev. Phys. Chem. 59 (2008) 463.
[5] I. Barth, J. Manz, Angew. Chem. 45 (2006) 2962.
[6] T. Zuo, A.D. Bandrauk, P.B. Corkum, Chem. Phys. Lett. 259 (1996) 313.
[7] A.H. Zewail, in: T. Frängsmyr (Ed.), Les Prix Nobel: The Nobel Prices 1999, Almqvist & Wiksell, Stockholm, 2000, pp. 110–203, and references therein.
[8] M. Drescher, M. Hentschel, R. Kienberger, M. Uiberacker, V. Yakovlev, A. Scrinzi, Th. Westerwalbesloh, U. Kleineberg, U. Heinzmann, F. Krausz, Nature 419 (2002) 803.
[9] H. Niikura, F. Légaré, R. Hasbani, M.Y. Ivanov, D.M. Villeneuve, P.B. Corkum, Nature 421 (2003) 826.
[10] T. Kanai, S. Minemoto, H. Sakai, Nature 435 (2005) 470.
[11] S. Baker, J.S. Robinson, C.A. Haworth, H. Teng, R.A. Smith, C.C. Chirilă, M. Lein, J.W.G. Tisch, J.P. Marangos, Science 316 (2006) 424.
[12] M.F. Kling, Ch. Siedschlag, A.J. Verhoef, J.I. Khan, M. Schultze, Th. Uphues, Y. Ni, M. Uiberacker, M. Drescher, F. Krausz, M.J.J. Vrakking, Science 312 (2006) 246.
[13] A.L. Cavalieri, N. Müller, Th. Uphues, V.S. Yakovlev, A. Baltuška, B. Horvath, B. Schmidt, L. Blümel, R. Holzwarth, S. Hendel, M. Drescher, U. Kleineberg, P.M. Echenique, R. Kienberger, F. Krausz, U. Heinzmann, Nature 449 (2007) 1029.
[14] J. Itatani, J. Levesque, D. Zeidler, H. Niikura, H. Pépin, J.C. Kieffer, P.B. Corkum, D.M. Villeneuve, Nature 432 (2004) 867.
[15] R. Santra, A. Gordon, Phys. Rev. Lett. 96 (2006) 073906.
[16] G. Jordan, A. Scrinzi, New J. Phys. 10 (2008) 025035.
[17] F. Remacle, R.D. Levine, Proc. Natl. Acad. Sci. USA 103 (2006) 6793.
[18] D. Geppert, P. von den Hoff, R. de Vivie-Riedle, J. Phys. B 41 (2008) 074006.
[19] L.S. Cederbaum, J. Chem. Phys. 128 (2008) 124101.
[20] T. Pfeifer, M.J. Abel, P.M. Nagel, A. Jullien, Z.-H. Loh, M.J. Bell, D.M. Neumark, S.R. Leone, Chem. Phys. Lett. 463 (2008) 11.
[21] A.H. Zewail, Annu. Rev. Phys. Chem. 57 (2006) 65. and references therein.
[22] P. Baum, D.-S. Yang, A.H. Zewail, Science 318 (2007) 788.
[23] N. Gedik, D.-S. Yang, G. Logvenov, I. Bozovic, A.H. Zewail, Science 316 (2007) 425.
[24] D.-S. Yang, C. Lao, A.H. Zewail, Science 321 (2008) 1660.
[25] D.J. Flannigan, P.C. Samartzis, A. Yurtsever, A.H. Zewail, Nano Lett. 9 (2009) 875.
[26] D.-S. Yang, A.H. Zewail, Proc. Natl. Acad. Sci. USA 106 (2009) 4122.
[27] S. Chen, M.T. Seidel, A.H. Zewail, Proc. Natl. Acad. Sci. USA 102 (2005) 8854.
[28] B.J. Siwick, J.R. Dwyer, R.E. Jordan, R.J.D. Miller, Science 302 (2003) 1382.
[29] J.R. Dwyer, C.T. Hebeisen, R. Ernstorfer, M. Harb, V.B. Deyirmenjian, R.E. Jordan, R.J.D. Miller, Phil. Trans. R. Soc. Lond. Ser. A 364 (2006) 741.
[30] H. Park, X. Wang, S. Nie, R. Clinite, J. Cao, Phys. Rev. B 72 (2005) 100301.
[31] C.-Y. Ruan, Y. Murooka, R.K. Raman, R.A. Murdick, Nano Lett. 7 (2007) 1290.
[32] P. Reckenthaeler, M. Centurion, W. Fuß, S.A. Trushin, F. Krausz, E.E. Fill, Phys. Rev. Lett. 102 (2009) 213001.
[33] P. Baum, A.H. Zewail, Proc. Natl. Acad. Sci. USA 104 (2007) 18409.
[34] G. Sansone, E. Benedetti, F. Calegari, C. Vozzi, L. Avaldi, R. Flammini, L. Poletto, P. Villoresi, C. Altucci, R. Velotta, S. Stagira, S. De Silvestri, M. Nisoli, Science 314 (2006) 443.
[35] E. Goulielmakis, M. Schultze, M. Hofstetter, V.S. Yakovlev, J. Gagnon, M. Uiberacker, A.L. Aquila, E.M. Gullikson, D.T. Attwood, R. Kienberger, F. Krausz, U. Kleineberg, Science 320 (2008) 1614.
[36] V.A. Lobastov, R. Srinivasan, A.H. Zewail, Proc. Natl. Acad. Sci. USA 102 (2005) 7069.
[37] S.A. Hilbert, C. Uiterwaal, B. Barwick, H. Batelaan, A.H. Zewail, Proc. Natl. Acad. Sci. USA 106 (2009) 10558.
[38] P.L. Kapitza, P.A.M. Dirac, Proc. Cambridge Philos. Soc. 29 (1933) 297.
[39] P.H. Bucksbaum, D.W. Schumacher, M. Bashkansky, Phys. Rev. Lett. 61 (1988) 1182.
[40] D.L. Freimund, K. Aflatooni, H. Batelaan, Nature 413 (2001) 142.
[41] B. Quesnel, P. Mora, Phys. Rev. E 58 (1998) 3719.
[42] B. Barwick, H.S. Park, O.-H. Kwon, J.S. Baskin, A.H. Zewail, Science 322 (2008) 1227. and references therein.
[43] E. Fill, L. Veisz, A. Apolonski, F. Krausz, New J. Phys. 8 (2006) 272.
[44] L. Veisz, G. Kurkin, K. Chernov, V. Tarnetsky, A. Apolonski, F. Krausz, E. Fill, New J. Phys. 9 (2007) 451.
[45] T. van Oudheusden, E.F. de Jong, S.B. van der Geer, W.P.E.M. Op't Root, O.J. Luiten, B.J. Siwick, J. Appl. Phys. 102 (2007) 093501.
[46] P. Baum, E. Riedle, M. Greve, H.R. Telle, Opt. Lett. 30 (2005) 2028.
[47] M. Bradler, P. Baum, E. Riedle, Appl. Phys. B 97 (2009) 561.
[48] P. Baum, A.H. Zewail, Proc. Natl. Acad. Sci. USA 103 (2006) 16105.
[49] D. Shorokhov, S.T. Park, A.H. Zewail, Chem. Phys. Chem. 6 (2005) 2228.
[50] L.-M. Peng, Micron 30 (1999) 625.
[51] F. van Bolhuis, P.B. Koster, T. Migchelsen, Acta Crystallogr. 23 (1967) 90.
[52] A. Pasternak, A. Anderson, J.W. Leech, J. Phys. C 10 (1977) 3261.
[53] A. Gahlmann, S.T. Park, A.H. Zewail, Phys. Chem. Chem. Phys. 10 (2008) 2894.
[54] G. Maroulis, C. Makris, U. Hohm, D. Goebel, J. Phys. Chem. A 101 (1997) 953.